1   *Article*

2 Identifying the Frequency Dependent Interactions
3 Between Ocean Waves and The Continental Margin
4 on Seismic Noise Recordings

5   **Zhen Guo [1], Yu Huang [1,2,*], Adnan Aydin [3] and Mei Xue [4]**

6   [1]   College of Civil Engineering, Tongji University, Shanghai 200092, China; zhenguo@tongji.edu.cn
7   [2]   Key Laboratory of Geotechnical and Underground Engineering of the Ministry of Education, Tongji
8   University, Shanghai 200092, China; yhuang@tongji.edu.cn
9   [3]   Department of Geology and Geological Engineering, The University of Mississippi, University, MS 38677,
10   USA; aaydin@olemiss.edu
11   [4]   State Key Laboratory of Marine Geology, Tongji University, Shanghai, 200092, China;
12   meixue@tongji.edu.cn
13   *   Correspondence: yhuang@tongji.edu.cn;

14   **Abstract:** This study presents an exploration into identifying the interactions between ocean waves
15   and the continental margin in the origination of double-frequency (DF, 0.1-0.5 Hz) microseisms
16   recorded at 33 stations across East Coast of USA (ECUSA) during a ten-day period of ordinary ocean
17   wave climate. Daily primary vibration directions are calculated in three frequency bands and
18   projected as great circles passing through each station. In each band, the great circles from all
19   stations exhibit largest spatial density primarily near the continental slope in the western North
20   Atlantic Ocean. Generation mechanisms of three DF microseism events are explored by comparing
21   temporal and spatial variations of the DF microseisms with the migration patterns of ocean wave
22   fronts in Wavewatch III hindcasts. Correlation analyses are conducted by comparing the frequency
23   compositions of and calculating the correlation coefficients between the DF microseisms and the
24   ocean waves recorded at selected buoys. The observations and analyses lead to a hypothesis that
25   the continental slope causes wave reflection, generating low frequency DF energy and that the
26   continental shelf is where high frequency DF energy is mainly generated in ECUSA. The hypothesis
27   is supported by the primary vibration directions being mainly perpendicular to the strike of the
28   continental slope.

29   **Keywords:** ocean waves; double-frequency microseisms; continental margin; continental slope
30

31   **1. Introduction**

32   Ambient noise (or seismic noise) has been widely used to estimate the seismic site effect
33   parameters (e.g. predominant frequency f_0, sediment thickness, amplification factor, etc.) of a site [1–
34   5] and to characterize both deep (down to the mantle of the Earth) and shallow (within the depth of
35   geological engineering activities) subsurface structures [6–15] for its advantages as a fast, effective
36   and reliable tool. However, the accuracies and reliabilities of the applications listed above would
37   strongly affected by the spatial and temporal variations of the ambient noise sources. One example
38   is given in [16] who estimated the amplification factors in Northern Mississippi of United States
39   applying the horizontal-to-vertical spectral ratio (HVSR, or Nakamura) method based on long term
40   ambient noise recordings. As the f_0s in their study region lie in the frequency band of ocean waves
41   induced double frequency (DF) microseisms (0.1–0.5 Hz), the estimated amplification factors (HVSR
42   values at f_0) fluctuate with time and are strongly correlated with the energy of the DF microseisms as
43   well as the ocean wave height. Many other studies suggest that if the noise sources are not
44   homogeneously distributed, the cross-correlation function cannot be reconstructed causing big errors

45   in subsurface tomography or even failure of subsurface tomography [17–22]. In addition, the ambient
46   noise with frequency greater than 0.1 Hz would be used in shallow subsurface tomography. From
47   this point of view, exploring the source locations, the spatial and temporal characteristics and the
48   generation mechanisms of the ambient noise with frequency greater than 0.1 Hz, especially the DF
49   microseisms, would significantly improve the application of the ambient noise in site effect
50   evaluation and shallow subsurface tomography.
51   In the spectrum of ambient noise recorded globally, the DF microseisms (or secondary
52   microseisms) manifest themselves as one or more energy peaks in the frequency band of 0.1–0.5 Hz
53   which is roughly twice of ocean waves' frequencies. It is widely accepted that DF microseisms are
54   generated by the non-linear interaction between ocean waves propagating in opposite directions with
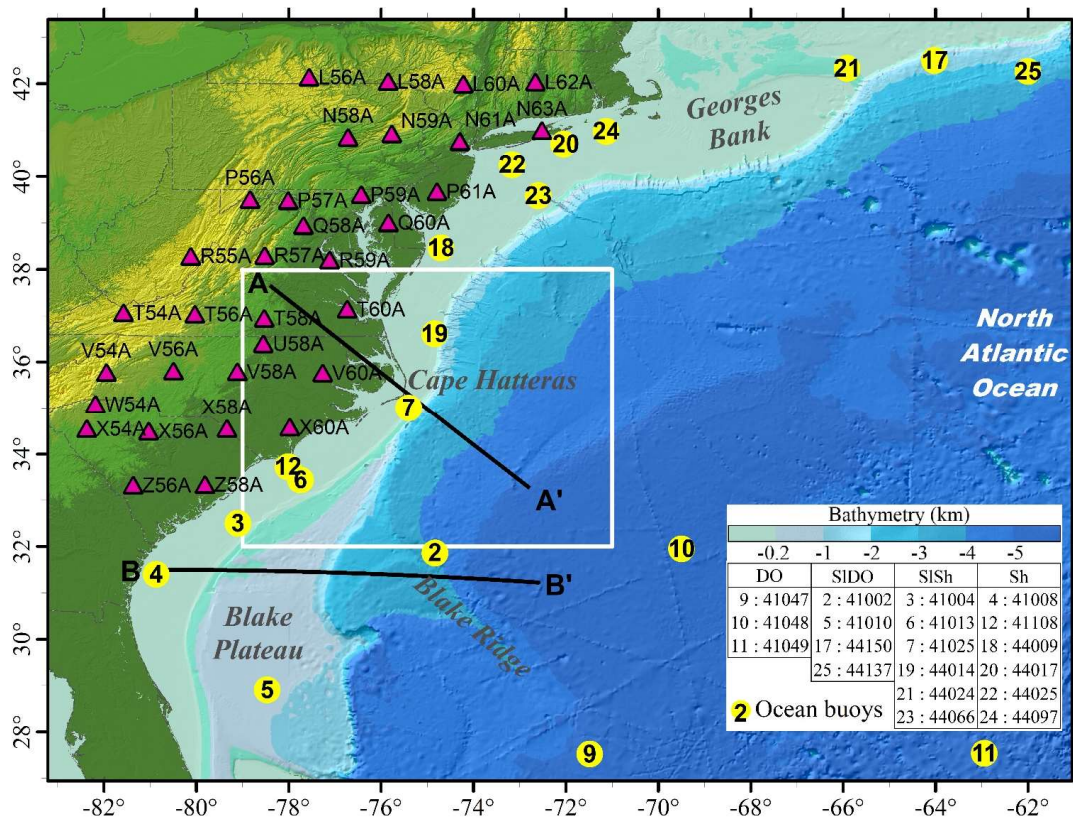55   similar frequencies (e.g. [23–31]).

Figure 1. Study area and locations of transportable array (TA) stations (triangles) and NOAA buoys
(yellow circles), recordings of which are analyzed in this study. The table lists the original numbers
and a simplified numbering scheme of the ocean buoys grouped according to their four distinct
locations: deep ocean (DO), the continental slope-deep ocean side (SlDO), the continental slope-shelf
side (SlSh) and the continental shelf (Sh). The color-encoded relief base map is from [32]. The black
lines A-A' and B-B' are the transects presented in Figure 8a and 8b. The white box indicates the area
where the underground shear velocity model (Figure 8c and 8d) was computed based on [15].

64   Recent studies suggest that two different circumstances may be responsible for generating
65   opposing ocean waves. The first group considers wave-wave interactions in the open-ocean during
66   strong storms [27,33–35]. However, DF microseisms can be observed worldwide even when there are
67   no strong storms locally or globally. This is explained by the second group of studies who emphasize
68   the role of interactions between the ocean waves and the continental margin, i.e. the ocean waves
69   being reflected at the coastal lines [22,36,37]. For example, [38] observed that Rayleigh waves in a
70   microseism recording at an ocean bottom seismometer in Pacific Ocean were approaching from
71   California coast during a super-typhoon rather than the location of the typhoon and concluded that
72   the microseisms were generated by interactions of typhoon-induced waves toward and their
73   reflections from the coastal line. In a different set of studies based on correlation analyses between

the ocean storms developed close to shorelines and the ambient noise recorded on coastal seafloor or costal land, it was recognized that the long- and short-period DF microseisms (LPDF, 0.085–0.2 Hz and SPDF, 0.2–0.5 Hz respectively) were excited by swells from distant and local waves respectively [25,30,31,39,40]. However, regarding the locations where the interactions (reflection) occur, there exist a debate in terms of the water depth (deep or coastal). [41] summarized the debate and compared theoretical and observed DF characteristics for each case considering the ocean wave frequency composition and velocities. It appears that the relationship between DF microseisms and ocean waves is not yet directly investigated as a function of water depth across the continental margin.

In this study, the continental slope, as a boundary between shallow (continental shelf) and deep (open ocean) water, is explored for its interactions with the ocean waves as well as its role and significance in the generation of DF microseisms. To reach this goal, the following data are utilized: (a) a total of 10-days of ambient noise data recordings from 33 seismic stations (Figure 1) of Transportable Array (TA) network along parts of the middle and southeastern North Atlantic coastal area and the Shenandoah Valley, (b) the WAVEWATCH III® (WWIII) hindcasts of ocean wave energy in Atlantic Ocean, and (c) ocean wave climate parameters recorded at relevant ocean buoys by National Data Buoy Center (NDBC) in Atlantic Ocean. While the selected recording period is free of major anomalous ocean activities (e.g. ocean storm, typhoon, hurricane) in Atlantic or Pacific Oceans (according to National Hurricane Center, NHC), it includes a few examples of relatively strong DF microseism events. Generation mechanisms of these events are explored by comparing temporal and spatial variations of the PSDs with the migration patterns of ocean wave fronts in WWIII hindcasts. For the entire period of microseism recordings, correlation analyses are conducted by comparing the frequency compositions of and correlation coefficients between DF microseisms and ocean wave parameters recorded at selected buoys.

2. Materials and Methods

2.1. Ambient noise data

The original time series in vertical (V), north-south (N) and east-west (E) directions are first parsed into 1-hour segments, followed by removing the mean, linear trend and instrument response in each segment [42]. Then each segment is processed following a 14-step procedure summarized below, to estimate the power spectral density (PSD) in horizontal (H) and vertical (V) directions (steps $1-5$), and the primary vibration direction by the radial-to-transverse spectral ratio (Ra) method (steps $6-10$) as well as the polarization analysis method based on [43] (steps $11-14$) in the three DF bands (DF1, 0.1–0.2 Hz; DF2, 0.2–0.3 Hz; and DF3, 0.3–0.4 Hz). The two methods used to estimate the primary vibration directions are both based on an assumption that DF microseisms propagate dominantly as a fundamental mode Rayleigh wave [34,44–46]. The Ra method searches the direction of the largest ratio of radial to transverse components on horizontal plane which is expected to be along the propagation direction of Rayleigh wave [29,42]. The polarization analysis method represents the particle motion within a short time range (when the propagation direction is reasonably stable) as an ellipsoid with three axes perpendicular to each other [43], from which the back azimuth of the major axis with highest probability for the whole recording period can be calculated. If the primary energy source is stable and strong enough, and significantly larger than secondary sources, the primary vibration directions obtained by the two methods would agree because the secondary sources do not alter direction of major axis but increase the Ra values in directions other than the major axis.

The steps of the data analysis are:

1. Apply an anti-triggering algorithm based on a prescribed range of short (1 s) to long (30 s) term average amplitude ratios (0.2 < STA/LTA < 2.5) to filter each segment for avoiding occasional energy bursts [4,47].

2. Apply fast Fourier transform with a 10% cosine taper on the filtered segments in three directions to calculate spectra ($V(f)$, $N(f)$, and $E(f)$) and then smooth them using Konno-Ohmachi method with a bandwidth coefficient of 40 [48].

124   3.   Calculate the resultant horizontal spectrum ($H(f)$):

$$H(f) = \sqrt{\frac{N(f)^2 + E(f)^2}{2}}, \tag{1}$$

126   4.   Compute the PSDs in vertical and resultant horizontal directions [49] in unit of (m/s²)²/Hz dB:

$$P(f) = 10\log\left[\frac{1}{0.825} \cdot \frac{2\Delta t}{N} \cdot Y(f)^2\right], \tag{2}$$

128   where $P(f)$ and $Y(f)$ are the PSD and spectral amplitude respectively in vertical or resultant
129   horizontal direction as function of frequency (f); Δt is the sample interval (0.01s); N is the
130   number of samples in each selected time-series segment; the constant 1/0.825 is a scale factor to
131   correct for the 10% cosine taper applied [50].

132   5.   Plot the PSDs of all segments at each station in time-frequency domain $PSD(t, f)$.

133   6.   Apply band-pass filter using the frequency bands, F = 0.1–0.2 Hz (DF1), 0.2–0.3 Hz (DF2) and
134   0.3–0.4 Hz (DF3) to each 1-hour segment to produce filtered amplitude-time series $V(t, F)$,
135          $N(t, F)$, and $E(t, F)$.

136   7.   Rotate the two horizontal components by an angle φ into radial (R) and transverse (T)
137   components [51] in each segment:

$$\begin{bmatrix} R(t, F, \varphi) \\ T(t, F, \varphi) \end{bmatrix} = \begin{bmatrix} -\cos(\varphi) & -\sin(\varphi) \\ -\sin(\varphi) & -\cos(\varphi) \end{bmatrix} \begin{bmatrix} N(t, F) \\ E(t, F) \end{bmatrix}, \tag{3}$$

139   in which φ is defined as the back-azimuth angle between the north and the radial direction from
140   the recording station toward the source.

141   8.   Calculate the root mean square of $R(t, F, \varphi)$ and $T(t, F, \varphi)$ in each segment and their ratio
142          $Ra(F, \varphi)$.

143   9.   Repeat steps 7 and 8 to calculate $Ra(F, \varphi)$ at every 1° increment of angle φ in 1°-360°.

144   10.   Calculate average values of $Ra(F, \varphi)$ for all segments at a station and determine the azimuth
145   φ_m for the maximum value of these averages. The angle φ_m is taken as the primary vibration
146   direction by Ra method.

147   11.   Further parse the filtered 1 hour segments in step 6 into ten 120 s windows and determine V_{ij},
148   N_{ij}, E_{ij}, where i = 1, 2 and 3 (separating DF1, DF2 and DF3 contents) and j = 1, 2, …, 30 (number
149   of windows). For each window, build the three-component covariance matrix **M**:

$$\mathbf{M}_{ij} = \begin{bmatrix} cov(V_{ij}, V_{ij}) & cov(V_{ij}, N_{ij}) & cov(V_{ij}, E_{ij}) \\ cov(N_{ij}, V_{ij}) & cov(N_{ij}, N_{ij}) & cov(N_{ij}, E_{ij}) \\ cov(E_{ij}, V_{ij}) & cov(E_{ij}, N_{ij}) & cov(E_{ij}, E_{ij}) \end{bmatrix}, \tag{4}$$

151   12.   Calculate the three eigenvalues λ_{ij} and associated eigenvectors $\vec{x}_{ij}$ of the covariance matrix
152          $\mathbf{M}_{ij}$ by solving:

$$\mathbf{M}_{ij}\vec{x}_{ij} = \lambda_{ij}\vec{x}_{ij}, \tag{5}$$

154   and define the maximum eigenvalue λ_{ij1}, and associated eigenvectors $(x_{ij_{11}} \quad x_{ij_{12}} \quad x_{ij_{13}})^\top$.

155   13.   Find the back azimuth angle φ_{ij} corresponding to the major axis of the polarized ellipse:

$$\begin{cases} \varphi_{ij} = \arctan\frac{x_{ij_{13}}}{x_{ij_{12}}} & if\ x_{ij_{11}} > 0 \\ \varphi_{ij} = \arctan\frac{x_{ij_{13}}}{x_{ij_{12}}} + 180 & if\ x_{ij_{11}} < 0 \end{cases}, \tag{7}$$

157   14.   Compute the probability of the back azimuth angle within 0°-360° range with a 10° bin width.
158   The back azimuth of highest probability is considered as the primary vibration direction by the
159   polarization method.

160   *2.2. Ocean data*

161   Theoretically, the frequencies of ocean waves that generate DF microseisms should be half of the
162   frequencies of DF peaks. Therefore, daily WWIII hindcast of $E(F/2)$ (log10(m²/Hz)) distributions within
163   the half frequency bands of corresponding DF peaks are used in this study in order to explore the
164   association between the ocean wave climates in Northern Atlantic Ocean and DF microseisms.
165   Additionally, a total of 19 ocean buoys in Atlantic Ocean (see Figure 1 for locations) are selected to
166   retrieve recordings of the ocean climate parameters including dominant wave period and significant
167   wave height (detailed descriptions of which can be found at NDBC website). In order to clearly display
168   the locations of the buoys on the figure and to facilitate discussion of the observations, these buoys are

169   renumbered and divided into four groups according to their locations (Figure 1): 1) deep ocean (DO)
170   buoys (9, 10 and 11); 2) the continental slope and deep ocean side (SlDO) buoys (2, 5, 17 and 25); 3) the
171   continental slope and shelf side (SlSh) buoys (3, 6, 7, 19, 21 and 23); and 4) the continental shelf (Sh)
172   buoys (the remaining ones).
173   In order for a direct comparison of frequency compositions of the ocean wave and DF microseisms,
174   the dominant ocean wave frequency of ocean waves at each buoy is simply doubled to determine the
175   double ocean wave frequency (DWF).

176   **3. Results**

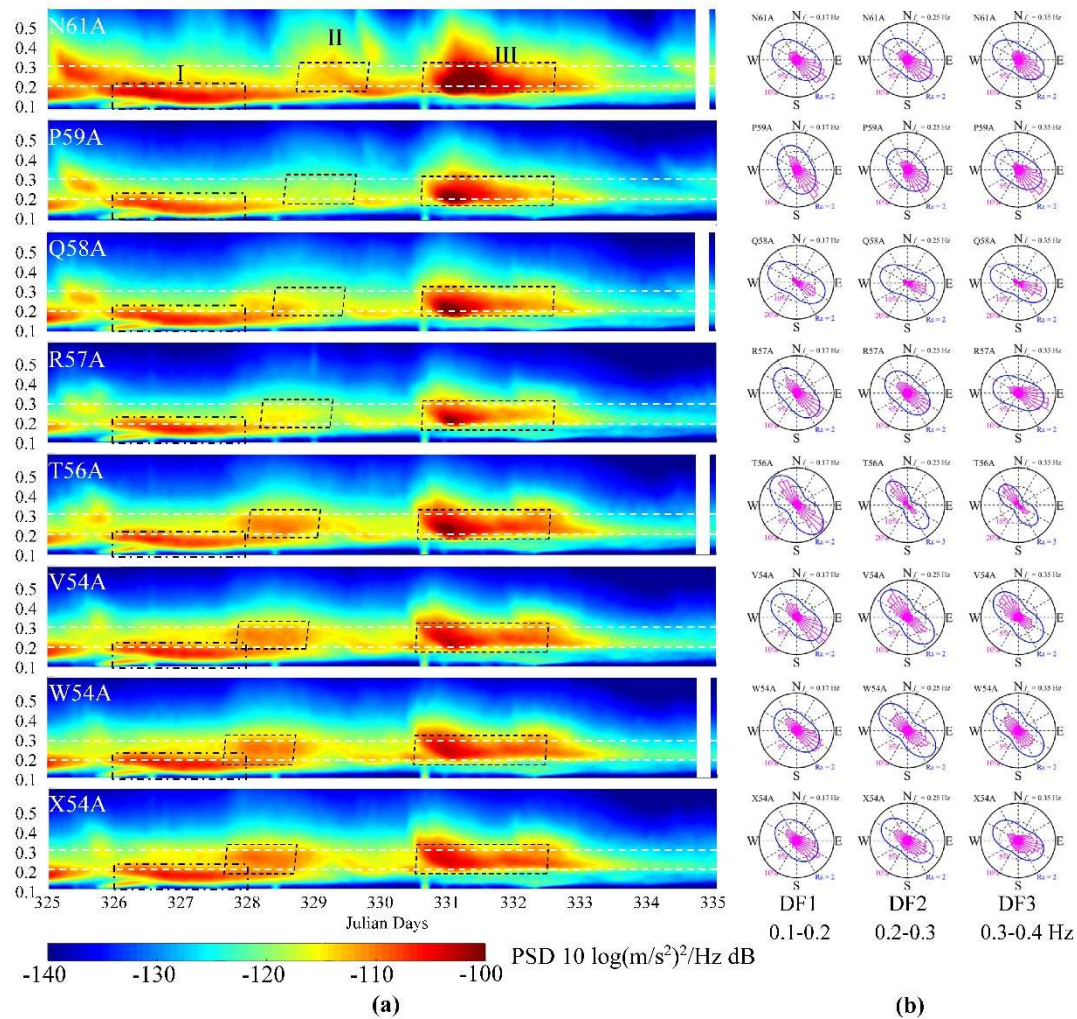177   *3.1. Power spectral density (PSD)*

Figure 2. (a) Power spectral density (PSD) plots in time-frequency domain of the vertical components at the selected stations. The dashed lines at 0.2 and 0.3 Hz mark the boundaries of the three frequencies ranges. Three relatively strong DF microseism events are identified and labeled as I, II and III. (b) Polar plots of average $Ra(\varphi)$ values (blue) combined with rose diagrams of back azimuths (calculated by the polarization analysis) (purple) at the three DF bands at the selected stations in the whole recording period. On each plot, the text labels refer to the recording station (e.g. N61A), central frequency of DF peak (e.g. 0.17 Hz), probability of back azimuth (in purple, e.g. 10%) and the scale of the solid outer circle in multiples of the $Ra(\varphi)$ value (in blue, e.g. $Ra = 2$). Same plots for the remaining stations are shown in Figure S1 in the supplement materials.

188   Figure 2a shows the vertical $PSD(t,f)$ plots at the stations selected to cover a wide latitude range
189   (40°N ~ 34°N) (see Figure 1 for locations of the stations). The remaining stations are divided into three
190   groups according to their locations (for their groups, see Figure S1a in the Supplementary Materials

191 to this article) and their $PSD(t, f)$ plots are shown in Figure S1b, S1d and S1f. In the recording time
192 period of this study, DF peaks are mainly in frequency band of 0.15 – 0.3 Hz at the selected example
193 stations, however, may cover a much wider frequency band at the stations close to the coastline (see
194 Figure S1b in the Supplementary Materials to this article). At all stations, three DF microseism events
195 with relatively high energy levels are identified and labeled with I, II and III which will be described
196 in section 3.3. Since DF microseisms exist continuously, clear starting and ending times for such
197 events cannot be determined precisely, which are therefore taken as the boundaries of high PSD level
198 periods (Figure 2a).

3.2. Primary vibration directions at DF peaks

200 Figure 2b presents the polar plots of average radial-to-transverse spectral ratios $Ra(\varphi)$ (blue
201 outline) and rose diagrams of back azimuths calculated by the polarization analysis (purple) in DF1,
202 DF2 and DF3 bands for the selected stations over the entire recording period of 10 days. The same
203 plots for the remaining stations are given in Figures S1c, S1e and S1g in supplementary materials.
204 The longer axis of each $Ra(\varphi)$ outline is identified indicating the average primary vibration direction
205 in ten days (φ_{m10}), which closely coincide with the major polarized direction.
206 The daily primary vibration directions (φ_{m1}) are calculated as well for all stations, and rose
207 diagrams of them in ten days are generated for the three DF bands in Figure 3. The main back-
208 azimuth in the three DF bands are shown to be in 110°–150°, which is perfectly consistent with the
209 results in the same area in [52].

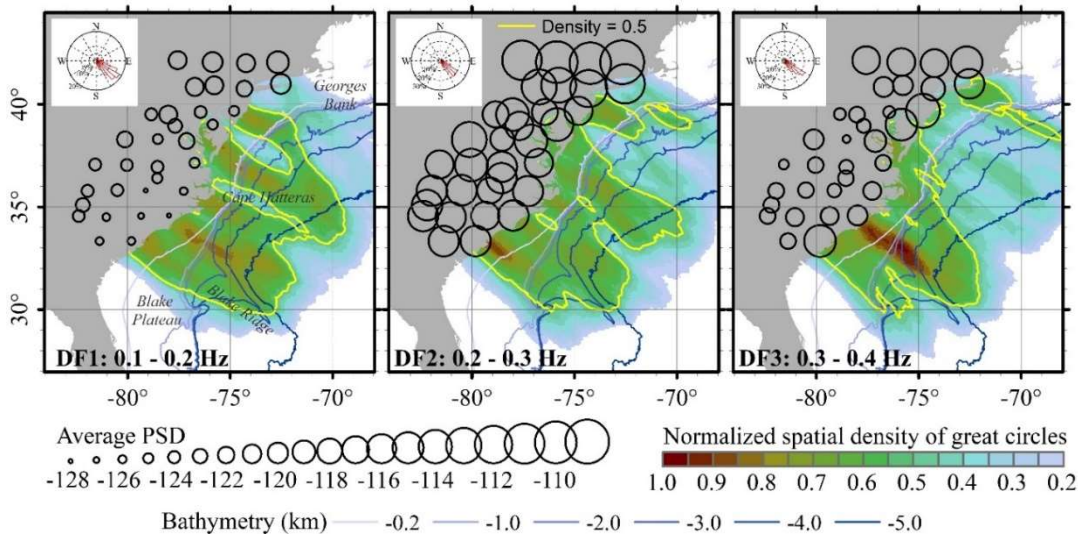**Figure 3.** The normalized spatial density (color gradient maps) of the great circles corresponding to
the daily primary vibration directions (φ_{m1}) and the vertical PSDs averaged for the entire recording
period (scaled circles) in the three DF bands. The yellow lines contour the density of 0.5. The rose-
diagram shows the probability distribution of all φ_{m1}s.

215 The great circles corresponding to all φ_{m1} are generated in the three DF bands. Any point on a
216 great circle can be considered as a possible energy source of the corresponding station in the
217 corresponding day and DF band. In order to find the possible source areas, spatial density of the
218 points sampled from the great circles with a sampling interval of 100 m are calculated, normalized
219 and plotted as color gradient map for each DF band in Figure 3, as well as the contours at density of
220 0.5 and the ocean bathymetries. The relative magnitude of the spatial density reflects the possibility
221 of the area to be energy source, i.e. the larger the density, the higher the possibility. Comparing the
222 three maps, it can be observed that the areas of high spatial density, e.g. the areas sketched by the
223 density contours of 0.5, shrink towards the continental shelf with increase of frequency, and the
224 spatial density in the area between Blake Ridge and Cape Hatteras is high in all three DF bands.

3.3. Excitation of the three relatively strong DF microseism events

226   First, the spectral WWIII hindcasts of ocean wave energy ($E(F/2)$ in log10(m²/Hz)) in North
227 Atlantic Ocean (see Figure S2 in the Supplementary Materials to this article) are used to explore the
228 temporal and spatial relationships in each frequency band of the energy levels between PSDs and
229 wave energy. This analysis demonstrates that 1) the primary vibration directions do not point to the
230 areas of high wave energy in open ocean, and 2) variations of ocean wave activities in open ocean of
231 North Atlantic Ocean have limited influence on the DF microseisms observed in east coast of United
232 States.
233   Based on the spatial density of great circles presented in Figure 3, it can be inferred that the
234 excitations of DF microseisms appear to be associated with the ocean waves in different areas of the
235 continental margin of the western North Atlantic Ocean. Therefore, the excitation mechanisms of the
236 three DF microseism events identified in Figure 2 are explored below with reference to area of the
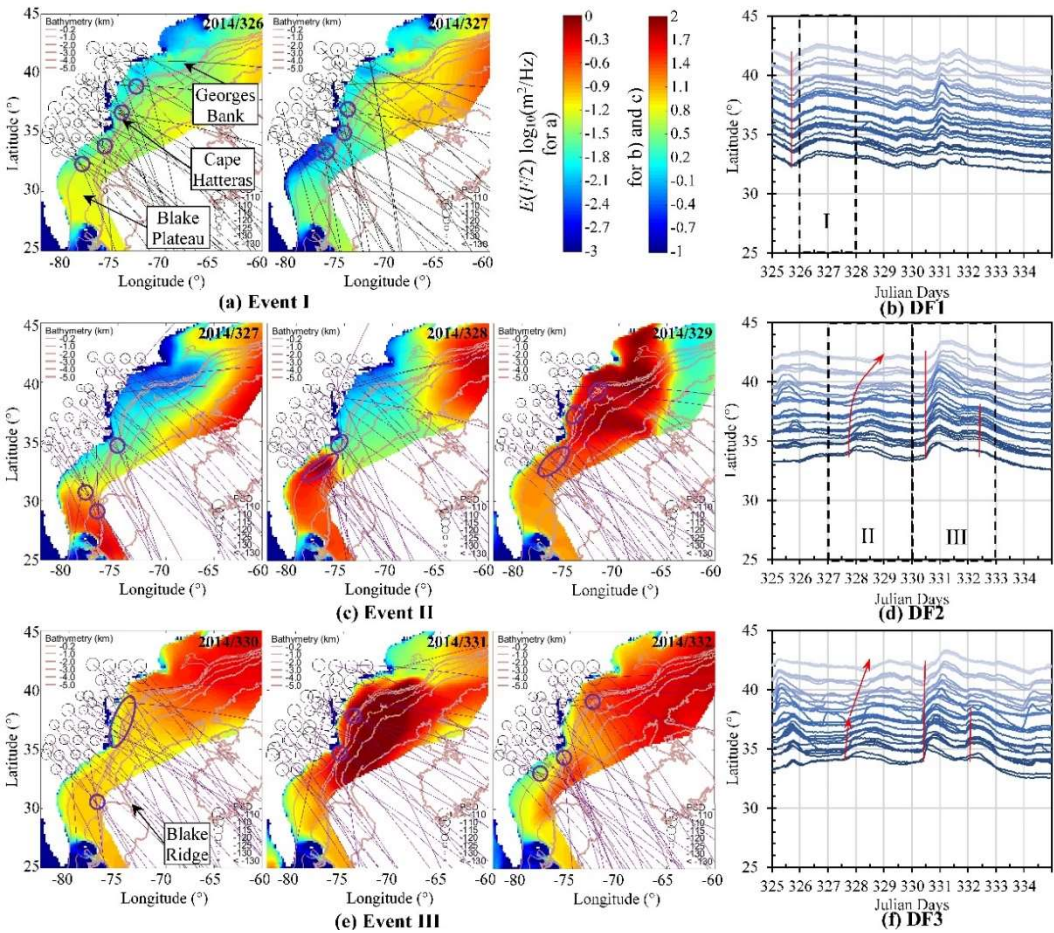237 continental margin as outlined in Figure 4.

Figure 4. (a), (c) and (d) Daily WAVEWATCH III hindcasts of ocean wave spectra ($E(F/2)$ in
log10(m²/Hz)) in Northern Atlantic Ocean (color gradient maps), PSD levels (small circles with scaled
sizes) and primary vibration directions (segments of great circles) at all stations corresponding to the
three events (I, II and III) identified in Figure 2. The purple circles/ellipses delimit the intersections of
the great circles; (d), (e) and (f) Time history of average PSDs in three frequency bands. In each plot,
the curves are stacked by the latitudes of the stations and the relief of each curve shows the change
of PSD level. The starting time of the three events are picked and connected to form the red lines, the
arrows of which show the impact sequence.

247   Figures 4a, 4c and 4e show the WWIII hindcasts of $E(F/2)$ in the western Northern Atlantic Ocean
248 (color gradient maps) within the half frequency band of events I, II and III identified in Figure 2. In
249 the corresponding days and frequency bands of the events, the PSD levels and the primary vibration
250 directions are demonstrated by the small circles with scaled sizes and segments of great circles
251 passing though the corresponding stations. The bathymetries of the western Northern Atlantic Ocean

252   are plotted as well in order to examine the importance of the continental slope in generation of DF
253   microseisms. In Figures 4b, 4d and 4f, the arrival times of each event are picked on the PSD-time plots
254   of all stations, and the connection of them form the red lines indicating the sequence of energy impact
255   on stations. In order to facilitate the description of the spatial variations of PSD levels and primary
256   vibration directions, the area where stations are placed are divided into two sections, north and south
257   of Cape Hatteras.

258   3.3.1. Event I

259   The energy of event I in DF1 band (LPDF, 01-0.2 Hz) starts to appear on late hours of day
260   2014/325 (red line on day 325 in Figure 4b) and reaches a higher strength on days 2014/326 and 327
261   (Figures 2 and 4b). The ocean waves in frequency band of 0.05-0.1 Hz in deep ocean close to the
262   continental slope are uniformly higher on day 326 than day 327, and extend to the continental slope
263   (Figure 4a). In addition, intersections of great circles concentrate at several small areas (purple circles)
264   evenly distributed on the continental slope on day 326. All these observations might explain the
265   occurrence of event I at the same time on day 326. The ocean wave energy decreases in the deep ocean
266   close to the continental slope and increase slightly at the deep ocean area south of Georges Bank on
267   day 327. The primary vibration directions at all stations cover a wider range, and the intersections of
268   great circles are not as concentrated as on day 326. These changes can explain the decrease of PSD
269   levels at most stations except for eight northernmost stations on day 327.

270   3.3.2. Event II

271   The event II in DF2 (0.2-0.3 Hz) band occurs on days 2014/327, 328 and 329, and arrives at the
272   stations in south section before north section as indicated by the curved red arrow in Figure 4d. This
273   sequence can be explained by the ocean wave interactions associated with the continental slope
274   (Figure 4c).
275   On day 327, the wave energy in frequency band of 0.1-0.2 Hz are relatively higher on lower Blake
276   Plateau (water depth 200-2000 m) and many great circles of the stations in south section intersect on
277   the edge of this area. The PSD levels at the stations in south section are roughly proportional to their
278   distances to lower Blake Plateau. Then on day 328 the wave front moves north along the continental
279   slope to south of Cape Hatteras while the wave energy increases to the highest. The great circles of
280   almost all stations in south section intersect in this area, and the PSD levels at these stations increase
281   significantly. On day 329, the wave front moves further north to the area between Georges Bank and
282   Cape Hatteras where the strike of the continental slope turns almost 90 degrees, causing the
283   significant increase of wave energy in this area. The great circles at the stations in north section do
284   not intersect in the open ocean where the wave energy are higher, but on the continental slope
285   segments south of Georges Bank and north of Cape Hatteras. The PSD levels at the stations to the
286   north increase but not as significantly as at the southern stations on day 328. The great circles at the
287   southern stations still intersect at the continental slope between Cape Hatteras and Blake Plateau but
288   not as concentrated as on day 328.

289   3.3.3. Event III

290   The event III in DF2 (0.2-0.3 Hz) band occurs on days 2014/330, 331 and 332, arrives at the stations
291   almost at the same time, but generates the energy peaks slightly earlier at the stations in south section
292   (Figure 4d). This sequence can also be explained by the ocean wave interactions associated with the
293   continental slope (Figure 4e).
294   On day 330, the great circles of most stations point to the area between Georges Bank and Blake
295   Plateau where the ocean waves are roughly in same height, and intersect evenly on this continental
296   slope segment. But the ocean wave energy on the continental slope of Georges Bank are relatively
297   higher which coincide well with the relatively higher PSD levels at the four northernmost stations.
298   On day 331, the ocean wave energy grows very fast while the wave front moves north quickly to
299   Georges Bank, resulting in high waves on the continental slope segment and deep ocean area between

300 Georges Band and Blake Ridge. Most intersections of the great circles align on this continental slope
301 segment and nearby deep ocean, and the PSD levels are very high at all stations. On day 332, the
302 wave front moves to northeast of Georges Bank and the wave energy decreases moderately.
303 However, the wave energy on the continental slope south of Georges Bank is still relatively high and
304 many great circles of the stations in northern section intersect here, which might be the reason of high
305 PSD levels at the eight northernmost stations. A new high wave front is developed at Blake Ridge
306 where most great circles of stations in southern section intersect, and a new PSD peak appears at the
307 stations in southern section.

308 *3.4. Correlation between DF microseisms and ocean wave parameters*

309 **Table 1.** Average correlation coefficients (CC) between the PSDs in the three DF bands and the
310 ocean wave heights in four groups of ocean buoys.

Stations	DF1 (0.1-0.2 Hz)				DF2 (0.2-0.3 Hz)				DF3 (0.3-0.4 Hz)			
	Sh	SlSh	SlDO	DO	Sh	SlSh	SlDO	DO	Sh	SlSh	SlDO	DO
L56A	0.283	0.248	**0.481**	-0.059	0.279	0.356	**0.520**	-0.267	0.305	0.320	**0.361**	-0.329
L58A	0.303	0.271	**0.492**	-0.080	0.293	0.365	**0.508**	-0.269	0.273	0.321	**0.361**	-0.297
L60A	0.292	0.258	**0.481**	-0.075	0.263	0.321	**0.486**	-0.259	0.272	0.290	**0.327**	-0.295
L62A	0.302	0.276	**0.515**	-0.094	0.247	0.305	**0.491**	-0.259	0.214	0.234	**0.303**	-0.255
N58A	0.305	0.265	**0.462**	-0.064	0.345	0.418	**0.486**	-0.286	0.373	**0.421**	0.339	-0.359
N59A	0.302	0.262	**0.456**	-0.086	0.335	0.398	**0.455**	-0.287	0.393	**0.407**	0.290	-0.366
N61A	0.314	0.283	**0.476**	-0.111	0.327	0.375	**0.451**	-0.292	**0.377**	0.353	0.254	-0.353
N63A	0.317	0.289	**0.546**	-0.102	0.283	0.326	**0.454**	-0.279	**0.284**	0.269	0.235	-0.298
P56A	0.289	0.241	**0.461**	-0.032	0.389	0.493	**0.535**	-0.227	0.457	**0.560**	0.416	-0.337
P57A	0.293	0.235	**0.425**	-0.035	0.382	0.462	**0.488**	-0.243	0.459	**0.536**	0.375	-0.355
P59A	0.309	0.260	**0.430**	-0.080	0.348	0.429	**0.445**	-0.261	0.414	**0.472**	0.294	-0.369
P61A	0.363	0.316	**0.492**	-0.125	0.355	**0.396**	0.327	-0.319	**0.403**	0.356	0.115	-0.388
Q58A	0.317	0.261	**0.379**	-0.063	0.409	**0.515**	0.466	-0.255	0.455	**0.566**	0.389	-0.328
Q60A	0.374	0.302	**0.456**	-0.080	0.340	**0.418**	0.306	-0.279	0.395	**0.397**	0.105	-0.381
R55A	0.295	0.242	**0.369**	-0.047	0.440	**0.537**	0.526	-0.223	0.468	**0.574**	0.450	-0.290
R57A	0.302	0.229	**0.380**	-0.025	0.428	**0.523**	0.509	-0.234	0.452	**0.571**	0.407	-0.317
R59A	0.303	0.243	**0.390**	-0.048	0.392	**0.479**	0.436	-0.243	0.419	**0.494**	0.265	-0.364
T54A	0.265	0.193	**0.311**	-0.017	0.428	0.540	**0.543**	-0.180	0.460	**0.580**	0.481	-0.230
T56A	0.289	0.234	**0.388**	-0.034	0.429	0.546	**0.526**	-0.188	0.444	**0.579**	0.454	-0.251
T58A	0.313	0.262	**0.404**	-0.046	0.415	0.540	**0.502**	-0.199	0.438	**0.573**	0.429	-0.282
T60A	0.335	0.293	**0.441**	-0.069	0.392	0.516	**0.437**	-0.224	0.405	**0.538**	0.323	-0.331
U58A	0.321	0.272	**0.403**	-0.041	0.415	**0.542**	0.508	-0.176	0.438	**0.580**	0.434	-0.267
V54A	0.289	0.223	**0.343**	-0.043	0.433	0.536	**0.563**	-0.154	0.457	**0.570**	0.504	-0.207
V56A	0.287	0.245	**0.385**	-0.050	0.437	**0.560**	0.548	-0.167	0.451	**0.584**	0.461	-0.234
V58A	0.312	0.253	**0.401**	-0.013	0.425	**0.549**	0.521	-0.154	0.438	**0.580**	0.450	-0.245
V60A	0.335	0.310	**0.424**	-0.048	0.402	**0.547**	0.484	-0.183	0.407	**0.567**	0.404	-0.277
W54A	0.276	0.221	**0.348**	-0.038	0.419	0.531	**0.564**	-0.139	0.465	**0.567**	0.514	-0.192
X54A	0.265	0.208	**0.314**	-0.031	0.421	0.534	**0.576**	-0.133	0.455	**0.559**	0.520	-0.184
X56A	0.288	0.232	**0.363**	-0.001	0.422	0.537	**0.551**	-0.112	0.447	**0.565**	0.509	-0.192
X58A	0.292	0.246	**0.403**	-0.017	0.430	**0.559**	0.542	-0.132	0.435	**0.578**	0.471	-0.222
X60A	0.315	0.284	**0.409**	0.001	0.420	**0.557**	0.524	-0.138	0.428	**0.581**	0.438	-0.245
Z56A	0.281	0.230	**0.365**	-0.008	0.403	0.507	**0.553**	-0.051	0.443	0.519	**0.546**	-0.127
Z58A	0.306	0.254	**0.395**	-0.034	0.468	0.554	**0.564**	-0.086	0.474	**0.569**	0.541	-0.164
Average	0.304	0.256	**0.418**	-0.051	0.382	0.478	**0.497**	-0.209	0.409	**0.492**	0.387	-0.283

See Figure 1 for the buoys in four groups. Sh: continental shelf; SlSh: shelf side of the continental slope; SlDO:
deep ocean side of the continental slope; and DO: deep ocean. Maximum CC values appear in bold.

311   In order to investigate the significance of the continental slope in the excitation of the DF
312 microseisms quantitatively, correlation analyses of time histories between DF microseisms and ocean
313 wave parameters recorded at the selected buoys in four groups (DO, SlDO, SlSh and Sh in Figure 1)
314 are carried out by considering the time-dependent variation of frequency composition and energy
315 levels.
316   The time histories of average PSDs in DF1, DF2 and DF3 bands are shown in Figures 4b, 4d and
317 4f respectively. The curves are stacked according to the latitudes of the stations and the reliefs show
318 the time-dependent variations of PSD levels. The double ocean wave frequencies (DWF) at the DO,
319 SlDO and SlSh buoys are closer to the frequency band of event I, and the waves whose DWFs match
320 events II and III are observed in groups SlDO, SlSh and Sh (for the time history of DWFs at the buoys,
321 see Figure S3 in the Supplementary Materials to this article). The correlation coefficients (CC) between
322 the time series of ocean wave height and PSD in the three DF bands are calculated for all pairs of
323 ocean buoy and ambient noise station, and the CC values are then averaged in each buoy group for
324 each DF band at each station, as summarized in Table 1. The bottom row of Table 1 gives the CC
325 values averaged for all stations. The CC values are normalized within the range [-1.0, 1.0], where
326 positive (negative) values represent same (opposite) trends of ocean wave height and PSD pairs and
327 the absolute value of CC express the level of consistency in these trends. In the DF1 band, better
328 correlations can be found between the DF microseisms at all stations and the ocean wave heights in
329 the continental slope on deep ocean side (SlDO). In the DF2 band, the DF microseisms at most stations
330 correlate well with the ocean wave heights in SlDO, and some with those in the continental slope on
331 shelf side (SlSh). In the DF3 band, higher CC values can be found in all SlDO, SlSh and continental
332 shelf (Sh) groups. Near-zero negative CC values for the deep ocean (DO) buoys implies that deep
333 ocean waves do not exert a positive influence on the DF microseisms.

4. Discussion

4.1. Hypothesis on the significance of continental slope for the origination of DF microseisms

336   The correlation analysis (Table 1) shows that the DF microseism trends in DF1, DF2 and DF3
337 bands are most compatible with the ocean wave activities in the continental slope on deep ocean side
338 (SlDO), the continental slope on both deep ocean and continental shelf sides (SlDO and SlSh), and
339 SlSh respectively. These domains of wave activities are separated by the continental slope, where
340 waves approaching from the deep ocean zone are reflected back creating non-linear wave-wave
341 interactions. This naturally leads to a hypothesis that the continental slope plays a significant role in
342 the origination of DF microseisms, and with increasing frequency band, the dominant origination
343 area migrates from SlDO to SlSh in east coast of United States. Validity of this hypothesis is explained
344 in detail in the following.
345   During the time period of event I (Figure 4a), the continental slope is shown to be the boundary
346 of impact from the ocean wave in frequency band of 0.05–0.1 Hz, the increase of wave energy in deep
347 ocean area south of Georges Bank does not cause increase of PSD levels at the stations in north section
348 but the decrease of ocean wave energy on the continental slope do coincide well with the decrease of
349 PSD levels in most stations from day 2014/326 to 327. Comparing events II and III (Figures 4c and 4e),
350 the PSD levels are much higher on day 331 than day 329, mainly because the higher wave energy on
351 the continental slope between Georges Bank and Blake Ridge on day 331. Figure 5 shows the
352 differences of the wave energy and PSD levels corresponding to DF2 band between day 331 and 329.
353 A coincidence can be found between the changes of PSD levels and wave energy on the continental
354 slope segment between the Georges Bank and Blake Ridge (outlined by the purple dash-dot line),
355 which supports the hypothesis.
356   Because no hurricane development was reported in Northern Atlantic Ocean during the period
357 of recordings analyzed in this study, most DF microseisms identified from these recordings should
358 be generated mainly by the non-linear interactions of incoming and reflected ocean waves of similar
359 frequencies. These interactions take place at different intensities and directions as determined by
360 ordinary ocean activities and ocean bottom topography. Theoretically strong reflections leading to

361 strong DF energy can occur only if the incoming waves encounter an obstacle perpendicular to their
362 propagation direction, as shown in Figure 6. The area and energy of constructive interaction is much
363 larger when the incoming wave direction is perpendicular (Figure 6b) than nearly parallel (Figure 6a)
364 to the obstacle. Considering that, in a reflection system, at each point of incidence at any angle, the
365 energy normal to the reflector is the largest (Figure 6b), a station receives strongest signal when the
366 station and incident point is aligned with the line normal to the reflector (Path A in Figure 6b). Such
367 an alignment should therefore correspond to the great circles (lines connecting the wave origination
368 areas to the stations) intersecting the continental slope nearly at orthogonal angles. In order to test
369 this hypothesis, the intersection angles δ between the great circles and the strike of the continental
370 slope are defined as shown in Figure 7a and the frequency histograms of δs in the three DF bands
371 are generated and shown in Figure 7b. The medians of δs in the three DF bands are 72.4°, 74.1° and
372 72.5° respectively, and the largest frequencies of occurrences are within 81°-90° range, which support
373 the proposed hypothesis.

374
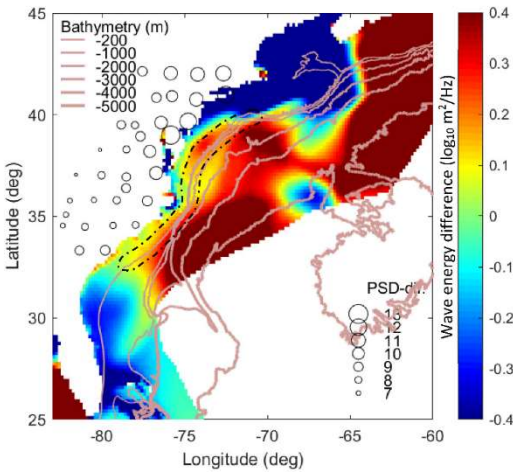
375 **Figure 5.** Difference of the ocean wave energy ($E(F/2)$ in $\log_{10}(\text{m}^2/\text{Hz})$) and PSD levels between day
376   329 and 331 (Figure 4c and 4e respectively).
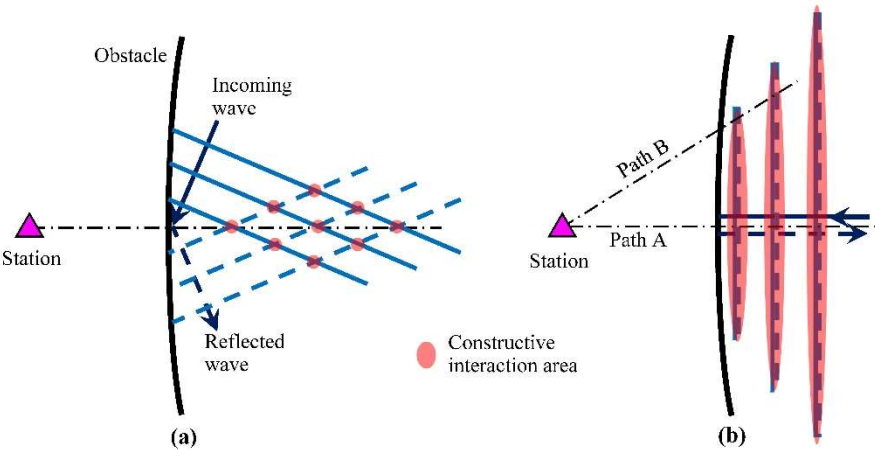
377

378 **Figure 6.** A sketch describing how constructive interactions of ocean waves and their reflections from
379   a barrier (the continental slope or the shoreline) can result in different energies when the angle of
380   incidence is (a) large and (b) 0°. Note a given station receives the strongest signals along the shortest
381   path A.

382   As the waves are reflected from the continental slope, the wave energy should be higher in the
383 continental slope and the nearby deep ocean zone than in the distant deep ocean zone and the
384 continental shelf. To examine this notion, the mean and standard deviation of ocean wave energy are
385 calculated in each of the four buoy groups, 2.19 and 0.44 m in DO, 2.48 and 0.98 m in SlDO, 2.10 and
386 0.99 m in SlSh and 1.57 and 0.74 m in Sh. The highest wave energy appears at the SlDO buoys and

387 then DO and SlSh buoys, which coincide well with areas of intersection of the great circle paths
388 (purple dashed ellipses in Figure 4). Similar observations can also be found in [33]. Recalling once
389 more that there was no strong storm in the northern Atlantic Ocean during the microseism
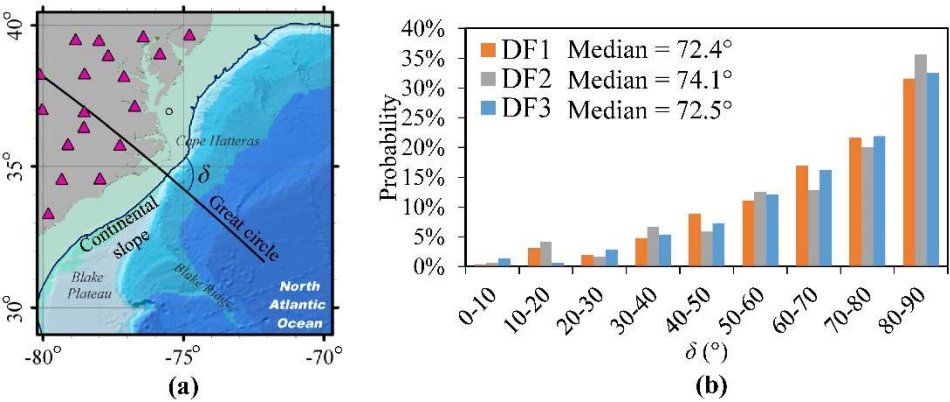390 recordings, the identified DF microseisms cannot be explained by ocean storms.

391

392 **Figure 7.** (a) Defining the angle δ ($< 90°$) between a great circle and the continental slope's strike, (b)
393 Histogram of the angles δs in the three DF bands.

394 The hypothesis is also supported by several ocean bottom observations in shallow and deep
395 waters divided by the continental slope. For example, [53] concluded that the excitation at DF peaks
396 require some part of the ocean storm to extend over the shallow water based on coherence studies.
397 Comparing ocean waves recorded in shallow waters (100 m deep) in Tasman Sea and microseisms
398 recorded near shoreline (30 km away from the ocean buoy) of North Island of New Zealand, [54]
399 observed that DF peaks were in > 0.2 Hz band when there was a local wind in the Tasman Sea but
400 lower than 0.2 Hz when the sea was calm and a swell from Southern Ocean arrived across the
401 continental slope. Another example is presented by [31]. Two pressure spectra were obtained from
402 two seafloor stations in the continental shelf (water depth of 0.6 km) and in the continental shelf edge
403 followed by a steep and deep continental slope (water depth of 1 km) respectively off the coast of
404 southern California (see topographic profiles in [55]). At the shallower site, a high spectral peak with
405 pressure level of around 10^3 Pa²/Hz was observed at around 0.2 Hz when a storm directly passed
406 overhead, whereas no spectral peak could be clearly identified when there was no passing storm. On
407 the deeper site, two high and sharp pressure spectral peaks appeared at 0.14 and 0.3 Hz with pressure
408 levels of $5×10^3$ and 10^4 Pa²/Hz respectively. Differences between the effects of shallow and deep ocean
409 on DF peaks' frequencies and energy levels presented in these studies imply that DF microseism in
410 the continental shelf is driven by local weather, whereas that in the deep ocean is excited by the
411 standing waves [35] generated by the interaction between the distant ocean swell and the waves
412 reflected due to the sudden change of water depth at the continental slope.

413 *4.2. Types of continental margin*

414 In this study, two types of continental margins are identified as exemplified by the transects A-
415 A' and B-B' (profile locations are marked in Figure 1) in Figure 8a and 9b respectively. Both types
416 have wide (~100 km) and shallow (< 0.2 km) shelves. Along the first type (A-A'), a high (~2.5 km) and
417 steep slope sharply change the profile followed by a long gentle slope (continental rise). In the second
418 type (B-B'), the shelf transition into the slope via a wide and gently dipping plateau (Blake Plateau)
419 followed by a shorter (~1.5 km) and gentler slope (than the first type), then a wide undulating plateau
420 (continental rise) ending with a relatively steep slope.
421 These differences between the continental margin profiles appear to modify the mechanism of
422 DF microseism generation as suggested by the consistently high spatial densities in the area covering
423 the Blake Ridge and northern Blake Plateau in all three DF bands (Figure 3). A more gradual
424 transition from the shelf and a shorter continental slope are the most prominent features that can
425 support generation of a relatively stable energy level in these areas. Concavity of the continental slope

426   at the edge of Blake Plateau potentially causes strong reflections resulting in higher DF energy. In
427   contrast, the continental slope at Cape Hatteras has a convex outline that could cause a diffraction
428   pattern, consequently a lower spatial density in this area as shown in the map of DF1 band in Figure
429   3. As the DF3 microseisms are generated in the continental shelf, the rough shoreline at Cape Hatteras
430   may be the reason for higher density observed in DF3 band in Figure 3.
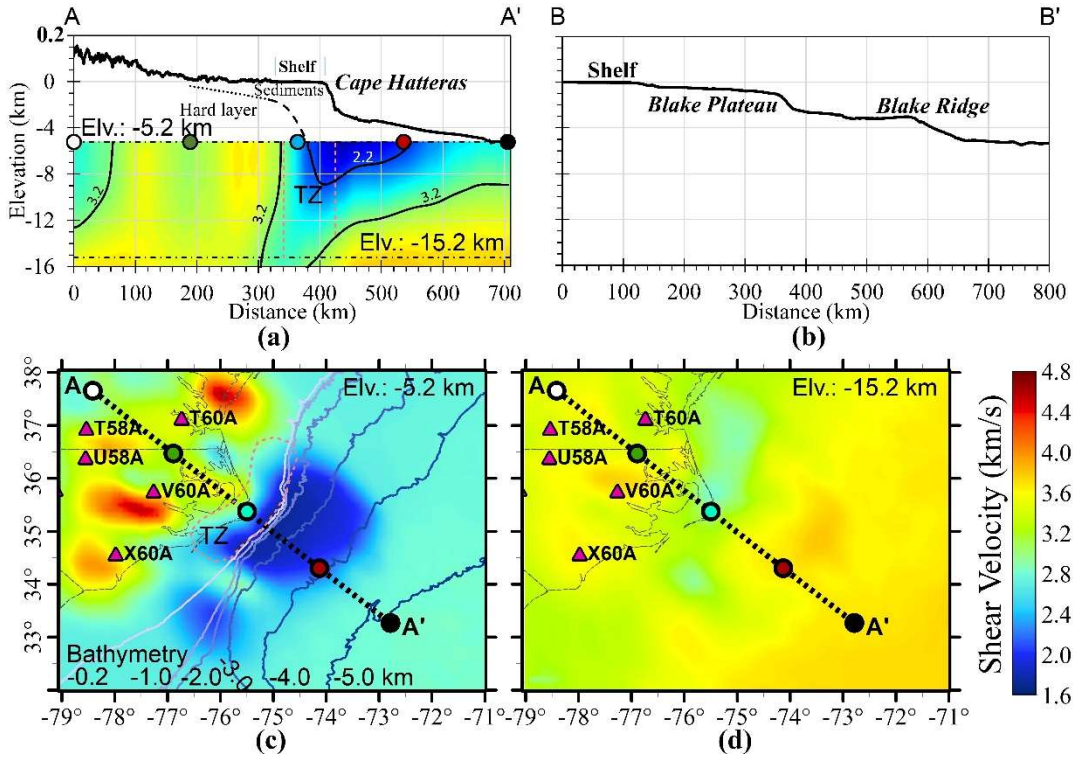
Figure 8. Topographic profiles of the continental margin along (a) A-A' and (b) B-B' (marked in Figure
1) based on General Bathymetric Chart of the Oceans (GEBCO, 2014). The shear velocity profile and
contours in (a) are based on [15]. The geophysical interface between sediments and bedrock is
estimated (black dotted line) by HVSR method and was extended seaward by inference (black dashed
line) to connect with the 2.2 km/s shear velocity contour. A transitional zone (TZ) with the largest
shear velocity gradient is identified and outlined by the two pink dashed lines in (a). The shear
velocity models inside the white box outlined in Figure 1 are generated for elevations (Elv.) of -5.2
km (c) and -15.2 km (d) based on [15].

440   Recent studies also support the hypothesis about the role of the continental slope and show that
441   submarine ridges act similarly to cause reflection of the waves. [56] by comparing the seasonal
442   variation of DF microseisms and ocean activities concluded that DF microseism in 0.15 – 0.2 Hz band
443   on the King George Island (on Antarctic Peninsula) originates from a region of Drake Passage instead
444   of the continental shelf around Antarctic Peninsula even though it is several times wider than that
445   around Cape Hatteras. The ocean at Drake Passage is at least 3 km deep and is delimited by the
446   continental slope of Antarctic Peninsula and an underwater ridge roughly normal to the slope. [33]
447   showed that the excitation locations of both P- and S-wave microseisms observed by a seismometer
448   array in Japan are distributed along the eastern continental slope of Greenland and Reykjanes Ridge
449   extended from Iceland into the deep ocean. An ocean bottom straight blocked by relief features [34,56]
450   promotes formation of ocean wave reflection at the continental slope.
451   The hypothesis may appear to fail the test based on the observations in [57], who compared the
452   DF spectra (around 0.15 Hz) at three seismometer stations in the coastal region of Oregon and
453   California with the ocean wave climate parameters' spectra (see their figure 17). Based on an excellent
454   correlation between DF peak and wave spectra, they concluded that DF microseism is generated by
455   the wave activities near the shoreline. Significantly different widths of the continental shelves, being
456   much narrower on the western continental margin of North America, and the location of the ocean

457 buoys being on the edge of such a narrow continental shelf (see their figure 15) can explain the
458 apparent failure. Together with the low frequency (< 0.2 Hz) of their DF peak, it can be argued that
459 DF microseism observed by [57] was also a result of the reflections from the nearby continental slope
460 as put forward in the proposed hypothesis.

461 *4.3. Rayleigh wave refraction*

462   As mentioned in "Data acquisition and processing" section, the Ra and polarization analysis
463 methods to estimate the primary vibration direction are based on an assumption that DF microseisms
464 propagates dominantly as fundamental mode Rayleigh waves. To verify this assumption, Figure 9 is
465 generated to show the probability distributions of the phase differences between the two orthogonal
466 horizontal components (φ_{HH}) and between the vertical and horizontal components on the primary
467 vibration direction (φ_{VH}) in the three DF bands. The facts that φ_{HH} is dominant in 0° and φ_{VH} is
468 mainly in 65°– 80° and -65°– -80° reveal that the energy is propagating as Rayleigh waves dominantly
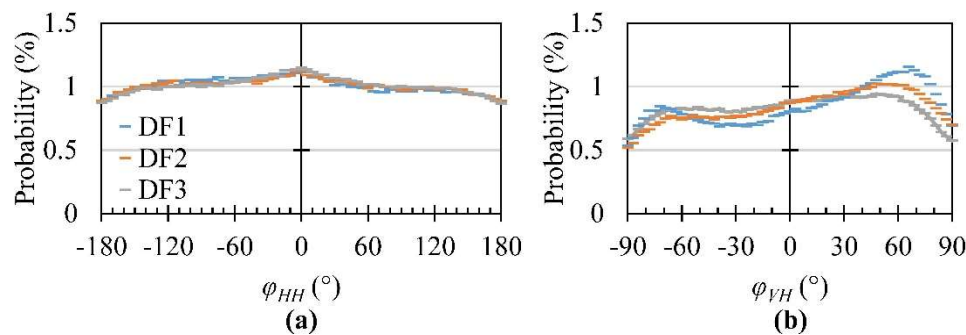469 [58], which coincides well with the observation in [52].

470

471   **Figure 9.** Probability distribution of the phase difference between (a) the two horizontal components
472   (φ_{HH}) and (b) the vertical and horizontal component on primary vibration direction (φ_{VH}).

473 4.3.1. Refraction at the water-solid earth interface

474   As explained by [59], when the energy in the DF band is generated from wave-wave interaction
475 in the ocean, it propagates as "pseudo-Rayleigh waves" (pRg) in water column and turns to free
476 surface Rayleigh waves (FSRW) when it reaches solid earth. In the water column, due to phase speed
477 difference, the pRg exists in different forms: dominantly elastic pRg in shallow water with phase
478 speed roughly equal to that of FSRW, and acoustic pRg in deep water with phase speed of about 60%
479 of FSRW. Definitions of shallow and deep waters vary with the wave frequencies. According to the
480 analysis in this study, the energy in LPDF (DF1) band is generated around the continental slope
481 where the water depth is generally smaller than 3000 m (Figure 1), especially on Blake Plateau (≤ 1000
482 m) and edge of Blake Ridge (~3000 m). According to figure 14 in [59], with the increase of frequency
483 from 0.1 Hz to 0.2 Hz, the depth in the water column of elastic pRg dominance decrease from 3000 m
484 to 1500 m, under which the elastic pRg transfer to fundamental acoustic pRg. Thus, phase-speed
485 difference might exist at the water-solid earth interface deeper than 1500 m, i.e. areas except Blake
486 Plateau, however, the DF energy would still propagate vertically in the water column and transfer to
487 solid earth. Even though there is significant energy loss at the interface, the spherical spreading of
488 the DF energy in the solid earth will not change. Therefore, the phase speed difference on the water-
489 solid earth interface is not likely to affect the determination of source location by great circle. For
490 high-frequency (0.2–0.5 Hz) DF band, the hypothesis put forward in this manuscript claims that the
491 energy is generated in the continental slope and continental shelf where the water depth is smaller
492 than 200 m. The same figure in [59] shows that the energy in this band should also propagate as elastic
493 pRg and directly transition to FSRW on the continental shelf. Because there is no significant phase
494 speed difference between elastic pRg and FSRW, Rayleigh wave refraction at the surface of solid earth
495 is not likely to be significant.

496 4.3.2. Refraction within the solid earth

497   The Rayleigh wave ray paths are expected to bend also when they travel through the solid earth
498   boundaries with significant impedance contrasts. In order to examine possibility of such boundaries
499   and implications for the validity of the triangulation method, the shear velocity (*Vs*) structure of the
500   study area is explored as described below.
501   The cross section A-A' presented in Figure 8a shows under the continental slope, there exists a
502   layer of material having *Vs* less than 2.2 km/s, which is interpreted as sediments in [15]. Our HVSR
503   survey around the eastern foothills of the Appalachian mountain and near the coastal area suggest
504   that the sediment-hard layer interface lies at a depth as depicted by a dotted line in the A-A' profile
505   in Figure 8a, and that the average *Vs* of the sediment is about 0.9 km/s [5]. According to [48], the shear
506   velocity contrast at the sediment-hard layer interface should be larger than 2.5 to produce a clear a
507   predominant frequency peak on HVSR spectrum, therefore, the *Vs* of the hard layer should be around
508   2.2 km/s. Therefore, this interface is inferred to connect to the 2.2 km/s contour line (depicted as the
509   dashed line in Figure 8a). Shear velocity gradients are calculated along A-A' at two different
510   elevations by [15] shear velocity model, and a transitional zone (TZ) of largest shear velocity gradient
511   (where *Vs* increases from about 1.7 to 3.2 km/s within a horizontal distance of ~80 km) is identified
512   and outlined as shown in Figure 8a. The TZ at Cape Hatteras (Figure 8c) extend roughly parallel to
513   the continental slope. The absence of notable shear velocity variations at -15.2 km (Figure 8d) suggests
514   that the transitional zone may not extend to this depth.
515   As explained above, the Rayleigh waves propagating through the solid earth from the deep
516   ocean near the continental slope (DF1 and DF2 bands) or from the continental shelf (DF3 band) to the
517   inland stations are expected to change propagation direction due to gradual and continuous
518   refraction as they pass through TZ. The total refraction angle ε is defined as shown in Figure 10a only
519   for the great circles passing through TZ which represents the worst scenario of changes. The
520   cumulative probability of ε in the three DF bands is given in Figure 10b. The weighted average (m)
521   of ε in DF1, DF2 and DF3 bands are calculated to be 8.8°, 8.2° and 8.7° respectively, and the
522   probabilities of ε values less than these corresponding weighted averages (P < m) are 60.2%, 63.1%
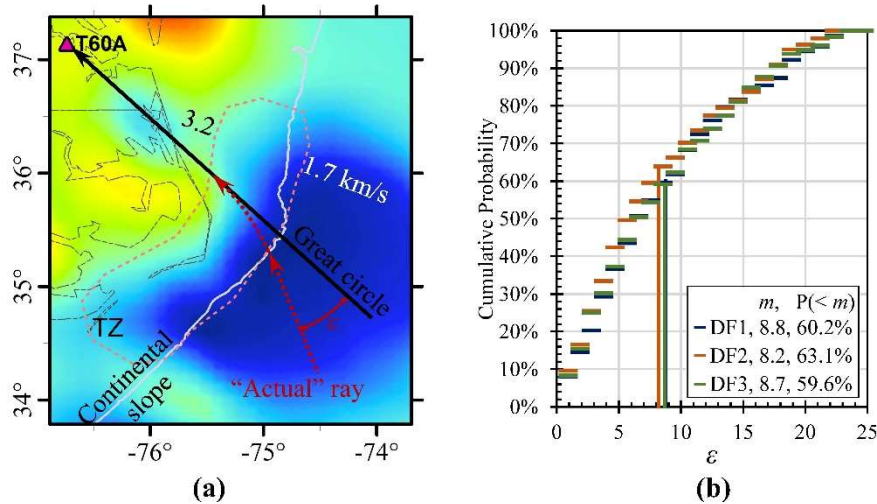523   and 59.6%.

524

Figure 10. (a) Defining angle ε to measure total refraction of Rayleigh wave ray passing through the
transitional zone (TZ in Figure 8a and 8c). The black solid and red dotted lines are the great circle
projected in this study and "actual" ray path of Rayleigh wave respectively. b) Cumulative
probability of ε for waves in the three DF bands propagating through TZ.

529   Another examination of the Rayleigh wave refraction from sediments to bedrock is carried out
530   by tracking hurricane "Sandy" in Atlantic Ocean on 27 October 2012 using 8 hours ambient noise
531   recorded on the bedrock in Tishomingo, Mississippi. DF peak is found at the central frequency of 0.18
532   Hz with very high energy. The primary vibration direction at this central frequency is calculated by
533   both *Ra* and Polarization analysis methods and projected as great circles which point to the locations
534   of hurricane "Sandy" successfully (see Figure S4 in the Supplementary Materials to this article). Thus

535   the great circles can be considered as valid projections to the source areas of the DF energy.

536   *4.3. Rayleigh wave refraction*

537   According to the hypothesis and the discussion above, the DF microseisms in LPDF (DF1) band
538   is generated in the deep ocean close to the continental slope and propagate to stations on land.
539   Depending on the location of the stations, the propagation paths are different, i.e. through sediments
540   and bedrock to stations on inland bedrock, and through sediments on coastal stations on sediments,
541   resulting in different attenuations and energy levels at stations. This difference is observed in this
542   study. In Figure 3, the PSD levels in DF1 band increase from coast (sediments) to inland (Appalachian
543   Mountain) while the distance to source (ocean) increase. The possible explanation is that the
544   attenuation due to spherical spreading is less effective than energy absorption in sediments. A similar
545   trend is observed by [52] in the same study area. In DF2 band, the PSD levels at coastal stations are
546   slightly larger than or equal to those at inland stations, which might because the attenuation due to
547   spherical spreading and absorption in sediments are equally effective. In DF3 band, the PSD levels at
548   coastal stations are obviously larger than those at inland stations, due to the attenuation is
549   dominantly spherical spreading and absorption effect is equally effective, which reveals that the DF
550   microseisms in this band is generated in continental shelf and propagates mainly in sediments.

5. Conclusions

551

552   This study explored the role and significance of the continental slope in the interactions between
553   the ocean waves and the continental margin as well as the resulted double-frequency (DF)
554   microseisms recorded in ENAM. The primary vibration direction analysis of the ambient noise
555   recordings in the study area shows that these DF microseisms originated in areas of the North
556   Atlantic Ocean, which are generally aligned in SE direction with the recording stations. The great
557   circles corresponding to these primary vibration directions for different DF peaks intersect at a
558   number of locations enabling delineation of source areas along the continental slope. Correlation
559   analysis between DF microseisms and ocean wave climate by considering the correspondence in their
560   frequency composition and variation in energy levels shows that the DF microseisms in DF1 (0.1–0.2
561   Hz), DF2 (0.2–0.3 Hz) and DF3 (0.3–0.4 Hz) bands correlate well with the ocean wave activities in the
562   continental slope on deep ocean side, and in the continental slope on both deep ocean and shelf sides,
563   and in the continental slope on the shelf side respectively. These analyses lead to a hypothesis on the
564   frequency dependent interactions of ocean waves with the continental margin and the origination of
565   DF microseisms. The steep continental slope is a key submarine topographic feature which behaves
566   as an obstacle causing reflections of the incoming low frequency ($\lesssim$ 0.15 Hz) ocean waves and
567   formation of standing waves to generate low frequency ($\lesssim$ 0.3 Hz) DF microseisms. While the high
568   frequency ($\gtrsim$ 0.15 Hz) ocean waves are reflected at the shallow portion of the continental shelf to
569   excite high frequency ($\gtrsim$ 0.3 Hz) DF microseisms. This hypothesis is also supported by the
570   observations that 1) the great circles corresponding to the primary vibration directions of DF
571   microseisms are mostly normal to the strike of the continental slope; and 2) the ocean wave energy
572   in the continental slope or the nearby deep ocean are higher than in the distant deep ocean and the
573   continental shelf. Additional systematic observations at different parts of the globe will help to
574   determine validity and limits of the proposed hypothesis under all possible climatic and bathymetric
575   conditions.

576   With the frequency dependent interactions between the ocean waves and the continental margin
577   determined, one could further analyze the possible mass wasting on the continental margin caused
578   by the ocean wave energy input and transmission while ocean waves interact with the continental
579   margin.

584 station groups, Figure S2: Daily WWIII hindcasts of spectral ocean wave height in Northern Atlantic Ocean (color
585 gradient maps), and PSD levels (small circles with scaled sizes) and primary vibration directions (great circles)
586 at all stations in the corresponding DF bands: DF1 in the top two rows, DF2 in the middle two rows, and DF3 in
587 the bottom two rows. The frequency band of ocean wave (half of corresponding DF band) and day are labeled
588 on top of each plot, Figure S3: Time history of double dominant ocean ocean wave frequencies (DWF) and
589 significant ocean wave heights (WH) at the ocean buoys grouped according to their locations, deep ocean (DO),
590 the continental slope on deep ocean side (SlDO), the continental slope on shelf side (SlSh) and the continental
591 shelf (Sh) (see Figure 1 for their locations and original names), Figure S4: An example to verify the validity of
592 great circle projecting to the sources of LPDF microseisms. The great circles at the station T2 on bedrock in
593 Tishomingo, Mississippi project to the sources of DF microseisms induced by hurricane "Sandy" on 27 October
594 2012 successfully.

595 **Author Contributions:** Conceptualization, Z.G.; methodology, Z.G.; formal analysis, Z.G.; investigation, Z.G.;
596 writing—original draft preparation, Z.G.; writing—review and editing, A.A., M.X. and Y.H.; funding
597 acquisition, Y.H. All authors have read and agreed to the published version of the manuscript.

608 **Conflicts of Interest:** The authors declare no conflict of interest. The funders had no role in the design of the
609 study; in the collection, analyses, or interpretation of data; in the writing of the manuscript, or in the decision to
610 publish the results.

611 References

612 1.   Nakamura, Y. A method for dynamic characteristics estimation of subsurface using microtremor on the
613   ground surface. *QR of RTRI* **1989**, 30, 25-33.
614 2.   Bodin, P.; Horton, S. Broadband microtremor observation of basin resonance in the Mississippi
615   embayment, Central US. *Geophys. Res. Lett*. **1999**, 26, 903–906.
616 3.   Bodin, P.; Smith, K.; Horton, S.; Hwang, H. Microtremor observations of deep sediment resonance in
617   metropolitan Memphis, Tennessee. *Eng. Geol.* **2001**, 62, 159-168.
618 4.   Bard, P.-Y.; SESAME-team. Guideline for the implementation of the H/V Spectral Ratio technique on
619   ambient vibrations-measurements, Processing and Interpretations. SESAME European Research Project
620   EVG1-CT-2000-00026, D23.12, **2005**.
621 5.   Guo, Z.; Aydin, A.; Kuszmaul, J. Microtremor recording in northern Mississippi. *Eng. Geol.* **2014**, 179, 146-
622   157.
623 6.   Lobkis, O.I.; Weaver, R.L. On the emergence of the Green's function in the correlations of a diffuse field. *J.
624   acoust. Soc. Am.* **2001**, 110, 3011–3017.
625 7.   Snieder, R. Extracting the Green's function from the correlation of coda waves: A derivation based on
626   stationary phase. *Phys. Rev. E*, **2001**, 69, 046610, doi:10.1103/PhysRevE.69.046610.
627 8.   Shapiro, N.M.; Campillo, M. Emergence of broadband Rayleigh waves from correlations of the ambient
628   seismic noise. *Geophys. Res. Lett*. **2004**, 31, L07614, doi:10.1029/2004GL019491.
629 9.   Shapiro, N.M.; Campillo, M.; Stehly, L.; Ritzwoller, M.H. High resolution surface wave tomography from
630   ambient seismic noise. *Science*, **2005**, 307, 1615–1618, doi:10.1126/science.1108339.
631 10. Sabra, K.G.; Gerstoft, P.; Roux, P.; Kuperman, W.A.; Fehler, M.C. Extracting time-domain Green's
632   function estimates from ambient seismic noise. *Geophys. Res. Lett.* **2005**, 32, L03310
633   doi:10.1029/2004GL021862.
634 11. Sabra, K.G.; Gerstoft, P.; Roux, P.; Kuperman, W.A.; Fehler, M.C. Surface wave tomography from
635   microseisms in Southern California. *Geophys. Res. Lett*. **2005**, 32, L14311, doi:10.1029/2005GL023155.

636   12.   Yang, Y.; Ritzwoller, M. Characteristics of ambient seismic noise as a source for surface wave
637   tomography. *Geochem. Geophys. Geosyst.* **2008**, 9, Q02008, doi:10.1029/2007GC001814.
638   13.   Yang, Y.; Ritzwoller, M.; Levshin, A.; Shapiro, N. Ambient noise Rayleigh wave tomography across Europe.
639   *Geophys. J. Int.* **2007**, 168, 259–274, doi:10.1111/j.1365-246X.2006.03203.x.
640   14.   Stephenson, W.J.; Hartzell, S.; Frankel, A.D.; Asten, M.; Carver, D.L.; Kim W.Y. Site characterization for
641   urban seismic hazards in lower Manhattan, New York City, from microtremor array analysis. *Geophys. Res.*
642   *Lett.* **2009**, 36, L03301, doi:10.1029/2008GL036444.
643   15.   Lynner, C.; Porritt R.W. Crustal structure across the eastern North American margin from ambient noise
644   tomography. *Geophys. Res. Lett.* **2017**, 44, 6651–6657, doi:10.1002/2017GL073500.
645   16.   Guo, Z.; Aydin A. A modified HVSR method to evaluate site effect in Northern Mississippi considering
646   ocean wave climate. *Eng. Geol.* **2016**, 200, 104-113.
647   17.   Stehly, L.; Campillo, M.; Shapiro, N.M. A study of the seismic noise from its long-range correlation
648   properties. *J. Geophys. Res.* **2006**, 111, B10306, doi:10.1029/2005JB004237.
649   18.   Shapiro, N.M.; Ritzwoller, M.H.; Bensen, G.D. Source location of the 26 sec microseism from cross-
650   correlation of ambient seismic noise. *Geophys. Res. Lett.* **2006**, 33, L18310, doi:10.1029/2006GL027010.
651   19.   Tsai, V.C. On establishing the accuracy of noise tomography travel-time measurements in a realistic
652   medium. *Geophys. J. Int.* **2009**, 178, 1555-1564, doi: 10.1111/j.1365-246X.2009.04239.x.
653   20.   Zeng, X.; Ni, S. A persistent localized microseismic source near the Kyushu Island, Japan. *Geophys. Res. Lett.*
654   **2010**, 37, L24307, doi:10.1029/2010GL045774.
655   21.   Ermert, L.; Villaseñor, A.; Fichtner, A. Cross-correlation imaging of ambient noise sources. *Geophys. J. Int.*
656   **2016**, 204, 347-364.
657   22.   Guo, Z.; Xue, M.; Aydin, A.; Ma Z. Exploring source regions of single- and double-frequency microseisms
658   recorded in eastern North American margin (ENAM) by cross-correlation. *Geophys. J. Int.* **2020**, 220, 1352–
659   1367.
660   23.   Longuet-Higgins, M.S. A theory for the generation of microseisms. *Philos. Trans. R. Soc.* London, **1950**, 243,
661   1-35.
662   24.   Hasselmann, K. A statistical analysis of the generation of microseisms. *Rev. Geophys. Space Phys.* **1963**, 1,
663   177-210.
664   25.   Bromirski, P.D.; Duennebier, F.K.; Stephen, R.A. Mid-ocean microseisms. *Geochem. Geophys. Geosyst.* **2005**,
665   6, Q04009, doi: 10.1029/2004GC000768.
666   26.   Essen, H.-H.; Krüger, F.; Dahm, T.; Grevemeyer I. On the generation of secondary microseisms observed
667   in northern and central Europe. *J. Geophys. Res.* **2003**, 108, no. B10, 2506, doi: 10.1029/2002JB002338.
668   27.   Obrebski, M.J.; Ardhuin, F.; Stutzmann, E.; Schimmel, M. How moderate sea states can generate loud
669   seismic noise in the deep ocean. *Geophys. Res. Lett.* **2012**, 39, L11601, doi: 10.1029/2012GL051896.
670   28.   Rhie, J.; Romanowicz, B. A study of the relation between ocean storms and the Earth's hum. *Geochem.*
671   *Geophys. Geosyst.* **2006**, 7, Q10004, doi: 10.1029/2006GC001274.
672   29.   Schimmel, M.; Stutzmann, E.; Ardhuin, F.; Gallart, J. Polarized Earth's ambient microseismic noise.
673   *Geochem. Geophys. Geosyst.* **2011**, 12, Q07014, doi: 10.1029/2011GC003661.
674   30.   Stephen, R.A.; Spiess, F.N.; Collins, J.A.; Hildebrand, J.A.; Orcutt, J.A.; Peal, K.R.; Vernon, F.L.; Wooding,
675   F.B. Ocean seismic network pilot experiment. *Geochem. Geophys. Geosyst.* **2003**, 4, 1092.
676   31.   Webb, S.C. Broadband seismology and noise under the ocean, *Rev. Geophys.* **1998**, 36, 105–142.
677   32.   Paskevich, V. srtm30plus-na_pctshade.tif - SRTM30PLUS color-encoded shaded relief image of North
678   America (approximately 1km) - GeoTIFF image: Open-File Report 2005-1001, U.S. Geological Survey,
679   Coastal and Marine Geology Program, Woods Hole Science Center, Woods Hole, MA, **2005**.
680   33.   Traer, J.; Gerstoft, P.; Bromirski, P.D.; Shearer P.M. Microseisms and hum from ocean surface gravity
681   waves. *J. Geophys. Res.* **2012**, 117, B11307, doi:10.1029/2012JB009550.
682   34.   Nishida, K.; Takagi, R. Teleseismic S wave microseism, *Science*, **2016**, 353 (6302). 919-921.
683   35.   Gerstoft, P.; Bromirski, P. "Weather bomb" induced seismic signals. *Science*, **2016**, 353 (6302). 869-870.
684   36.   Elgar, S.; Herbers, T.H.C.; Guza, R.T. Reflection of ocean surface gravity waves from a natural beach. *J.*
685   *Phys. Oceanogr.* **1994**, 24, 1503–1511.
686   37.   Ardhuin, F.; Stutzmann, E.; Schimmel, M.; Mangeney, A. Ocean wave sources of seismic noise. *J. Geophys.*
687   *Res.* **2011**, 116, C09004, doi:10.1029/2011JC006952.
688   38.   Sutton, G.; Barstow, N. Ocean bottom microseisms from a distant supertyphoon. *Geophys. Res. Lett.* **1996**,
689   23, 499-502.

39. Bromirski, P.D.; Flick, R.E.; Graham, N. Ocean wave height determined from inland seismometer data: implications for investigating wave climate change in the NE Pacific. *J. Geophys. Res.* **1999**, 104, C9, 20753-20766.

40. Dorman, L.M.; Schreiner, A.E.; Bibee, L.D.; Hildebrand, J.A. Deep-water seafloor array observations of seismo-acoustic noise in the eastern Pacific and comparisons with wind and swell, in Natural Physical Source of Underwater Sound, B. Kerman (Editor). Springer, New York, New York, **1993**, pp. 165–174.

41. Ebeling, C.W. Chapter One–inferring ocean storm characteristics from ambient seismic noise: A historical perspective. *Adv. Geophys.* **2012**, 53, doi: 10.1016/B978-0-12-380938-4.00001-X.

42. Guo, Z.; Aydin, A. Double-frequency microseisms in ambient noise recorded in Mississippi. *Bull. Seismol. Soc. Am.* **2015**, 105, 1691-1710.

43. Park, J.; Verono III, F.L.; Lindberg, C.R. Frequency dependent polarization analysis of high-frequency seismograms. *J. Geophys. Res.* **1987**, 92, no. B12, 12664-12674.

44. Cessaro, R.K. Sources of primary and secondary microseisms. *Bull. Seismol. Soc. Am.* **1994**, 84, 142-148.

45. Friedrich, A.; Krüger, F.; Klinge, K. Ocean-generated microseismic noise located with the Gräfenberg array. *J. Seismol.* **1998**, 2, 47-64.

46. Nishida, K.; Kawakatsu, H.; Fukao, Y.; Obara, K. Background Love and Rayleigh waves simultaneously generated at the Pacific Ocean floors. *Geophys. Res. Lett.* **2008**, 35, L16307, doi: 10.1029/2008GL034753.

47. Bard, P.-Y. Microtremor measurements: A tool for site effect estimation? Proc. 2nd Int. Symp. on the Effects of Surface Geology on Seismic Motion, Yokohama, Japan, 1-3 December **1998**, 1251-1279.

48. Konno, K.; Ohmachi, T. Ground-motion characteristics estimated from spectral ratio between horizontal and vertical components of microtremor. *Bull. Seismol. Soc. Am.* **1998**, 88, 28-241.

49. McNamara, D.E.; Buland, R.P. Ambient noise levels in the continental United States. *Bull. Seismol. Soc. Am.* **2004**, 94, 1517-1527.

50. Bendat, J.S.; Piersol, A.G. Random data: Analysis and measurement procedures, Wiley-Interscience, New York, USA, **1971**.

51. Havskov, J.; Ottemoller, L. Routine data processing in earthquake seismology, Springer, New York, New York, **2010**, 347 pp.

52. Koper, K.D.; Burlacu, R. The fine structure of double-frequency microseisms recorded by seismometers in North America. *J. Geophys. Res.* **2015**, 120, doi: 10.1002/2014JB011820.

53. Babcock, J.M.; Kirkendall, B.A.; Orcutt, J.A. Relationship between ocean bottom noise and the environment. *Bull. Seismol. Soc. Am.* **1994**, 84, 1991-2007.

54. Kibblewhite, A.C.; Ewans, K.C. Wave-wave interactions, microseism, and infrasonic ambient noise in the ocean. *J. Acoust. Soc. Am.* **1985**, 78, 981-994.

55. Schreiner, A.E.; Dorman, L.M. Coherence lengths of seafloor noise: Effect of ocean bottom structure. *J. Acoust. Soc. Am.* **1990**, 88. 1503-1514.

56. Lee, W.S.; Sheen, D.H.; Yun, S.; Seo, K.W. The origin of double-frequency microseism and its seasonal variability at King Sejong Station, Antarctica. *Bull. Seismol. Soc. Am.* **2011**, 106, 1446-1451.

57. Bromirski, P.D.; Duennebier, F.K. The near-coastal microseism spectrum: Spatial and temporal wave climate relationships. *J. Geophys. Res.* **2002**, 107, B8, 2166, doi: 10.1029/2001JB000265.

58. Koper, K.D.; Hawley, V.L. Frequency dependent polarization analysis of ambient seismic noise recorded at a broadband seismometer in the central United States. *Earthq. Sci.* **2010**, 23, 439-447.

59. Bromirski, P.D.; Stephen, R.A.; Gerstoft, P. Are deep-ocean-generated surface-wave microseisms observed on land? *J. Geophys. Res.* **2013**, 118, 3610–3629, doi:10.1002/jgrb.50268.